J. Fluid Mech. (2007), *vol.* 575, *pp.* 399–424. © 2007 Cambridge University Press
doi:10.1017/S0022112006004083 Printed in the United Kingdom

Shock-wave/expansion-wave interactions and the transition between regular and Mach reflection

R. HILLIER

Department of Aeronautics, Imperial College London, London SW7 2AZ, UK

(Received 2 May 2006 and in revised form 2 October 2006)

This paper presents numerical simulations for the interaction of an expansion wave with an incident shock wave of the opposite family, the specific aim being to study the resultant reflection of the now-perturbed shock wave from a solid surface. This problem is considered in the context of an incident flow entering a parallel duct, a situation that commonly arises in a range of flow-turning problems including supersonic intake flows. Once the incident shock conditions are such that Mach reflection must occur, it is shown that stabilization of a simple Mach reflection is only possible for a narrow range of Mach numbers and that this depends sensitively on the relative streamwise positioning of the origins of the shock wave and the expansion wave.

1. Introduction

Figure 1 shows a classical duct flow where a supersonic stream is turned, by a single plane shock wave, from one uniform state to another. This often represents an idealization for intake flows, in which case the 'incident' stream M_1 would usually be the flow downstream of another compression system. Focusing a plane shock exactly upon the concave corner, however, is a unique design condition that is unlikely to be realizable in practice. The off-design situation, where the incident shock wave impinges downstream of the corner and is then distorted by a corner expansion fan is the subject of this study.

Shock-wave reflection from a solid surface, and the transition between regular and Mach reflection, has been the subject of extensive study for both steady and unsteady flows. The steady case is appropriate here and the classical test configuration for virtually all studies is the wedge-generated shock wave, as shown in figure 2. There are two limiting criteria relating the wedge angle δ_W and the approach Mach number M_1 for the regular-to-Mach transition, both originally proposed by von Neumann (1943). These are the so-called detachment criterion and the mechanical-equilibrium criterion. The latter, usually now referred to as the von Neumann criterion, was essentially re-introduced by Henderson & Lozzi (1975, 1979). Figure 3 presents the (M_1, δ_W)-domain for a perfect gas with $\gamma = 1.4$; the transition boundaries for the two criteria are indicated and also the dual-solution domain, where both regular reflection and Mach reflection are theoretically possible. The interception between the two criteria occurs at Mach number 2.202, according to Molder (1979). The dual-solution region leads to the possibility of a hysteresis process, first suggested by Hornung, Oertel & Sandeman (1979) (see also Ben-Dor *et al.* 2002 for a more extended discussion). Experimental studies show a sensitivity to test conditions and stream disturbance, so that although Hornung & Robinson (1982) found that the

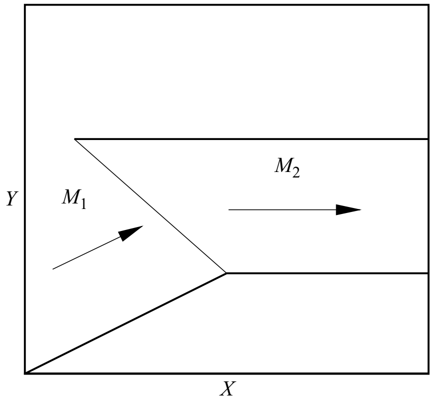

FIGURE 1. Simple schematic for the flow at the inlet to a duct turning from one uniform state to another through a single plane shock wave focused on an expansion corner.

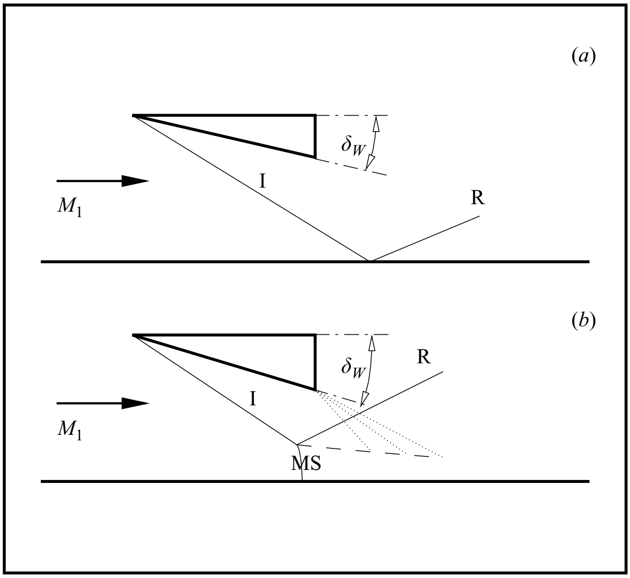

FIGURE 2. Schematic for classical shock-wave reflection, both (*a*) regular reflection and (*b*) Mach reflection. I, incident shock wave; R, reflected shock wave; MS, Mach stem; δ_W, wedge angle.

transition, regular to Mach or vice versa, always occurred at the von Neumann condition, other studies achieved the dual-solution state (e.g. Chpoun *et al.* (1995), although some questions were raised concerning the two-dimensionality of their flow). In computational fluid dynamics (CFD) studies, which are precisely two-dimensional and therefore effectively disturbance free, it has generally been observed (e.g. Ivanov *et al.* 1998; Ben-Dor *et al.* 1999) that if the wedge angle δ_W is progressively increased from below the lower (von Neumann) boundary then transition occurs at the upper, detachment, limit. When the initial deflection is above the detachment criterion, a reduction in wedge angle only causes a transition to regular reflection at the lower von Neumann boundary.

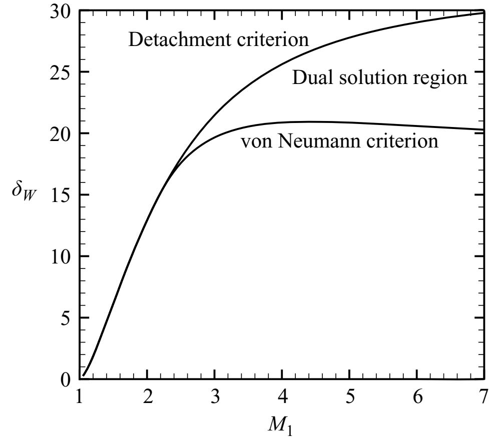

FIGURE 3. Polar plot for shock-wave reflection for the configuration of figure 2.

The streamtube downstream of the Mach stem is subsonic. The expansion wave that originates from the trailing edge of the wedge controls (provided that it is strong enough) the sonic throat in this streamtube and, in consequence, the characteristics of the upstream Mach stem. Various models have been proposed to predict the scale of the Mach stem for the wedge-induced incident shock wave (e.g. Azevedo & Lui 1989, the most detailed so far being due to Li & Ben-Dor 1997). The factors that determine the location and scale of the Mach stem turn out to be especially important for the duct shock-wave–expansion-wave interaction case; these are explored in detail in the present paper.

2. Modelling the shock–expansion interaction with the method of characteristics

For the off-design case, the shock-wave reflection at the lower wall is determined by a post-shock flow that has been turned towards the wall and also accelerated by the influence of the expansion wave. This important condition has not been documented to any extent other than in a short study by Li & Ben-Dor (1995).

The distortion of an incident shock wave by an expansion wave was modelled initially by the rotational method of characteristics. The basic configuration for the interaction is shown in figure 4. Here, interactions with the upper and lower surfaces of the duct are excluded, so that there is no relevant length scale and the data depend only upon the polar angle, ϕ, which is referenced to an origin at the expansion corner; ϕ_{LE} and ϕ_{TE} define the angles for the leading edge and trailing edge of the expansion fan. The initial (pre-shock) expansion field is a simple wave region (where only the C^+ characteristics are significant). Downstream of the shock wave the wave field is non-simple and rotational, with compatibility conditions along the two families of characteristics C^+ and C^-, defined respectively by (see Liepmann & Roshko 1957)

$$\mathrm{d}(\nu - \delta) = -\frac{\sqrt{M^2-1}}{\gamma R M^2}\mathrm{d}(s), \tag{2.1}$$

$$\mathrm{d}(\nu + \delta) = -\frac{\sqrt{M^2-1}}{\gamma R M^2}\mathrm{d}(s). \tag{2.2}$$

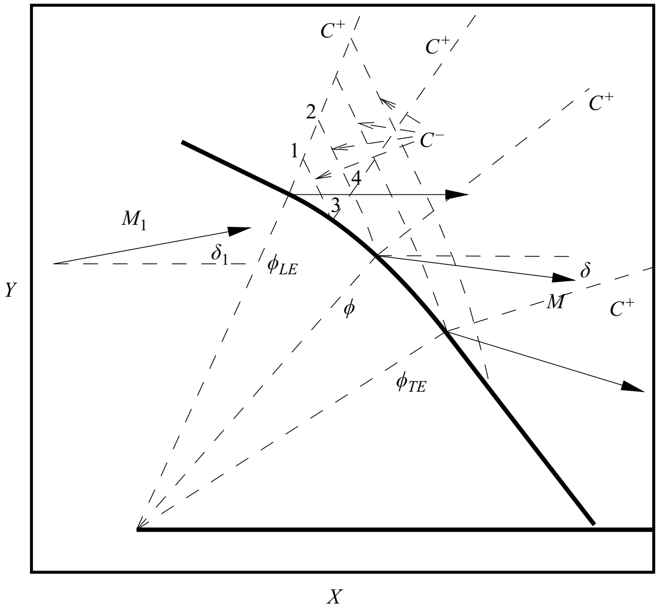

FIGURE 4. Schematic showing the interaction of a centred expansion wave with an incident shock wave. The angle ϕ is measured from an origin at the expansion corner. ϕ_{LE} and ϕ_{TE} denote the leading and trailing edge of the initial expansion wave. All angles are measured relative to the X-axis.

Here ν is the Prandtl–Meyer angle, δ is the local flow angle, R is the gas constant and s is the entropy. In this region the C^+ characteristics transmit information away from the shock wave, as indicated in the schematic of figure 4. The C^- characteristics essentially arise from the reflection of the outgoing C^+ characteristics by the rotational flow downstream of the curved shock wave; they transmit information from the post-shock flow field up to the shock wave, as shown.

The solution for the characteristics starts with an initial data curve produced by an equal-interval discretization along the first significant C^+ characteristic (originating from $\phi = \phi_{LE}$) that radiates into the post-shock flow; the conditions along this characteristic, and hence its trajectory, are simply determined from the known constant initial post-shock state. These data points provide the origin of the C^- characteristics and the point where these characteristics terminate at the shock wave provides the start point for all subsequent C^+ characteristics. The characteristic construction demonstrated in figure 4 is very coarse. For this construction the C^- characteristic from node 1 on the initial data curve is projected directly up to the shock wave at node 3. The appropriate shock-wave slope at node 3, and hence also the shock-wave position, is determined by satisfying the jump conditions across the shock wave and also (2.2) between nodes 1 and 3. The C^- characteristic from node 2 first solves (2.1) and (2.2) for the location and values at the ‘interior’ node 4, requiring the (now known) values at nodes 2 and 3 together with an interpolation, for the entropy at node 4, from the so-far-constructed flow field (employing the constancy of entropy along a streamline). The next step with this C^- characteristic is the calculation of the end shock point. As further start points are taken on the initial data curve, so the extent of the computed shock front increases. All node computations, both ‘interior’ and shock points, require an iterative solution, which is continued until successive node-Mach-number estimates change by less than 10^{-6}.

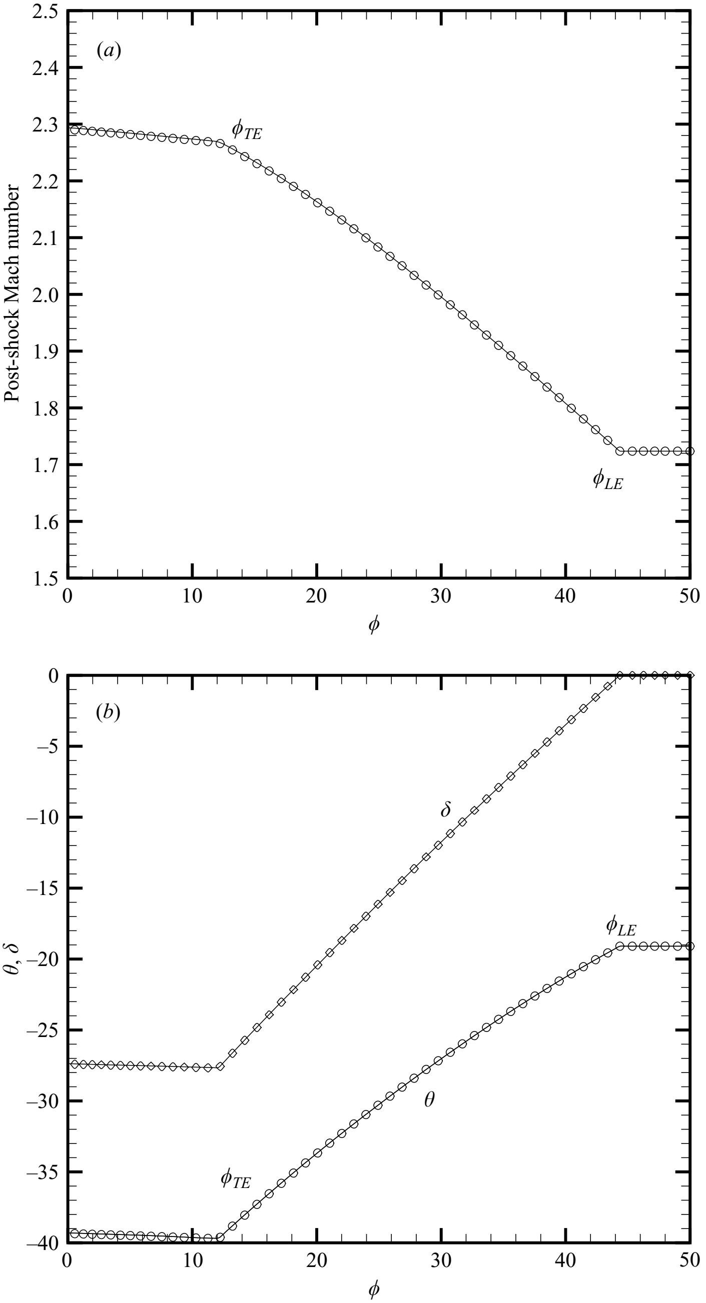

FIGURE 5. Convergence assessment for the MOC computations, for the example of a flow with $M_1 = 3.0$, $\delta_1 = 24.89$ degrees; the flow properties presented are those immediately downstream of the shock wave. The solid lines represent computation with 400 points along the perturbed shock front; the symbols represent a computation with 50 points. (*a*) Post-shock Mach number; (*b*) post-shock flow angle δ and shock-wave angle θ. The shock-wave angle θ is measured relative to the horizontal datum and the other quantities are defined in figure 4.

Figure 5 presents data, immediately post-shock-wave, for an example Mach-3.0 flow, the simulation extending to the position $\phi = 0$ which would be the lower surface of the duct. The solid lines and discrete symbols provide computations with 400 and

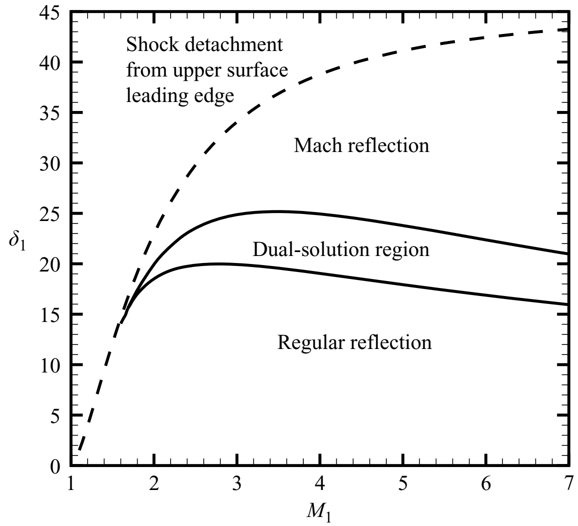

FIGURE 6. Interaction between an expansion wave and a shock wave, of the opposite family, showing the variation in the predicted angle for transition between regular and Mach reflection, according to the von Neumann criterion (lower solid curve) and the detachment criterion (upper solid curve).

50 points respectively along the perturbed shock front. All later modelling uses at least 400 points so that the method of characteristics (MOC) simulations can be regarded as mesh-converged. Note that slight changes occur in the post-shock properties in the region $\phi \leqslant \phi_{TE}$ because of the manner of formation of the C^- characteristics, by internal reflection of the C^+ characteristics from the rotational flow.

Using the MOC to determine the conditions, post-shock-wave, at impingement upon the reflection surface (i.e. along the ray $\phi = 0$), transition boundaries may be predicted from the detachment and von Neumann criteria; see figure 6. The figure also includes the boundary for detachment of the incident shock wave from the upper-surface (i.e. shock-generator) leading edge.

The interception between the von Neumann and detachment criteria occurs at $M_1 \approx 1.69$. Above this Mach number the domain is subdivided into three reflection zones: the bottom zone, where only regular reflection is possible; the top zone, where only Mach reflection should be possible; and an intermediate zone, where both Mach reflection and regular reflection appear to be possible. The maximum deflection angles are 25.2 degrees (at $M_1 \approx 3.5$) and 20.0 degrees (at $M_1 \approx 2.76$), for the detachment and von Neumann criteria respectively. The detachment criterion extends slightly below $M_1 \approx 1.69$, but the MOC had to be terminated at $M_1 \approx 1.59$ since the 'weak' incident-shock-wave solution then provides a subsonic post-shock flow, so that a solution for the characteristics is no longer possible. In the narrow region $1.59 \leqslant M_1 \leqslant 1.69$, therefore, the transition from regular to Mach reflection has to occur at the detachment criterion and is followed almost immediately by detachment of the incident shock wave from the upper-surface leading edge.

3. CFD modelling and the regular-reflection case

Detailed Euler computations were carried out using a second-order finite-volume Godunov-type method, implemented on a structured mesh of quadrilateral cells; the cell-interface fluxes were evaluated using the generalized Riemann problem of Ben-Artzi & Falcovitz (1984). This methodology has been applied by the present author to a range of problems involving complex interactions between shock waves and vortex sheets; see, for example Hillier (1991).

The streamwise extent of the domain for all computations occupied $-0.05H \leqslant x \leqslant 3.8H$, the leading edge of the upper shock-generating surface being at $x = 0.0$, $y = H$, where H is the duct height. Because of numerical 'smearing', an abrupt large-angle deflection (i.e. one approximating a truly centred expansion) at the lower expansion corner generates entropy errors in the layers of cells closest to the wall. This effect is virtually eliminated by turning the flow progressively (in a circular arc) over a short streamwise distance of $0.04H$. The expansion-surface position in the later computations then refers to the front of this segment. The cells are rectangular, apart from in the immediate vicinity of the expansion corner. A constant cell size $\Delta x = 0.0025H$ is used in the x-direction (1540 cells). For the upper 80% of the domain the cell size in the y-direction is constant at $\Delta y = 0.0025H$. A gradual refinement in Δy is employed as the lower surface is approached, to maintain resolution for various short-Mach-stem cases. At the lower wall $\Delta y = 0.000\,312\,5H$, with a total number of 480 cells in the y-direction.

The mesh boundary conditions are shown in the schematic of figure 7(a). The upstream (inflow) boundary at $X = -0.05H$ is held fixed at the free-stream condition. This is also imposed at the lower boundary of the domain, between $X = -0.05H$ and the expansion corner. The downstream boundary is treated as a continuative outflow condition; this is exact for the regular-reflection case since the exit flow is fully supersonic. It is also exact for many Mach-reflection cases where a sonic throat forms in the streamtube downstream of the Mach stem. For some cases a sonic throat cannot be formed and there is a mixed outflow, with regions of subsonic and supersonic flow. In these cases the outflow condition still appears satisfactory, and some examples of this will be demonstrated later. The short segment $-0.05 \leqslant X/H \leqslant 0$, $Y = H$ is also treated as an outflow boundary.

The preceding mesh describes the 'standard' case. Comparative coarse-mesh computations doubled Δx and Δy, and an assessment of mesh convergence for the regular-reflection case may be made from the density contours presented in figure 8. The flow deflection was just 0.5 degrees below the detachment criterion of figure 6 and therefore provides a sensitive operating condition. The simulations were started impulsively, imposing the free-stream condition everywhere as the initial state. The finer resolution of the incident and reflected shock waves using the standard mesh is clear, but in fact there are only small discrepancies in contour detail between the two cases. The residual errors associated with the expansion-corner modelling are equally small. Exact Prandtl–Meyer theory requires that the total pressure P_0 is preserved through the expansion. The maximum errors in figure 8 occur in the surface layer of cells, giving $P_0/P_{0,\infty}$ equal to 99.2% and 98.6% for the standard and coarse meshes, respectively. A detailed view of the flow field near the expansion corner, for the case of figure 8(b), is shown in figure 7(b).

4. CFD modelling of Mach reflection

4.1. *Expansion corner at* $X/H = 0.2$, $M_1 = 2.0$

In Mach reflection, stabilization of the Mach stem requires the formation of a sonic throat in the post-Mach-stem streamtube, otherwise downstream disturbances can propagate upstream to the Mach stem and alter its scale and location. In classical

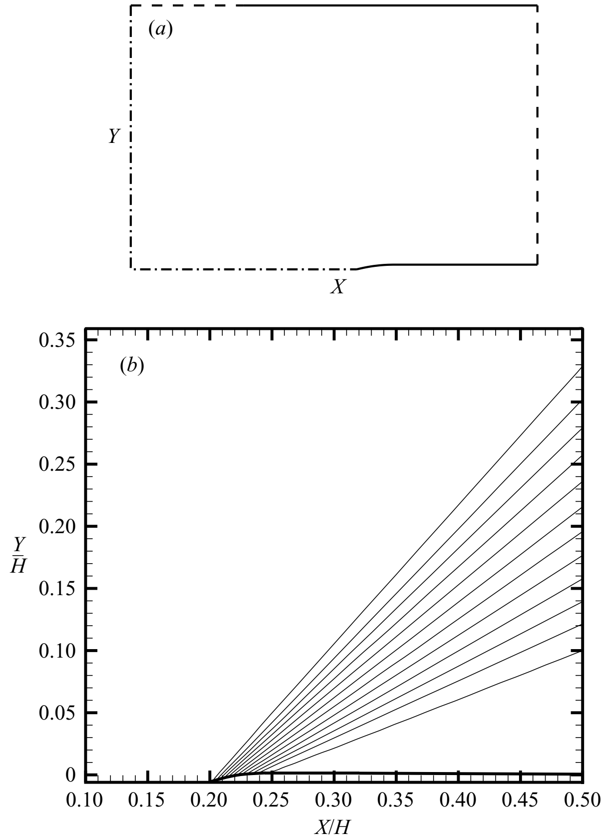

FIGURE 7. (a) Schematic showing boundaries of the computational domain: solid line, solid-surface boundary condition; dash-dotted line, fixed-inflow boundary condition; dashed line, continuative-outflow condition. (b) Density contours, in 5% intervals in ρ/ρ_∞, showing details for the case $M_1 = 2.0$, $\delta_1 = 19.44$ degrees, with the expansion corner at $X/H = 0.2$.

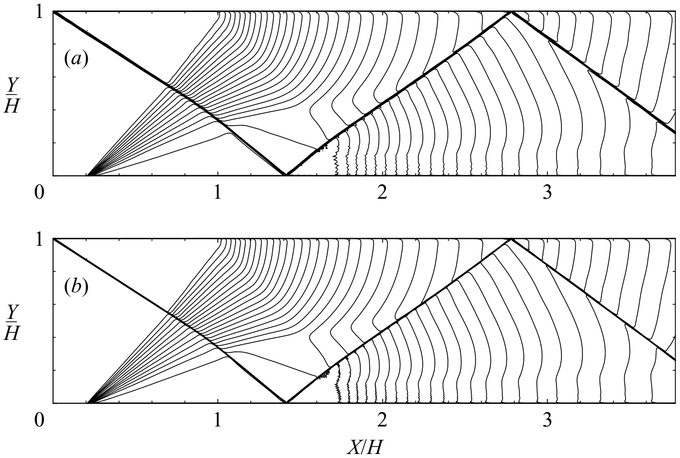

FIGURE 8. Density contours for regular reflection, with a Mach-2.0 flow deflected through 19.44 degrees and with the expansion corner at $X/H = 0.2$: (a) coarse mesh; (b) standard mesh. Both cases present the same contour increment of 5% intervals in ρ/ρ_∞.

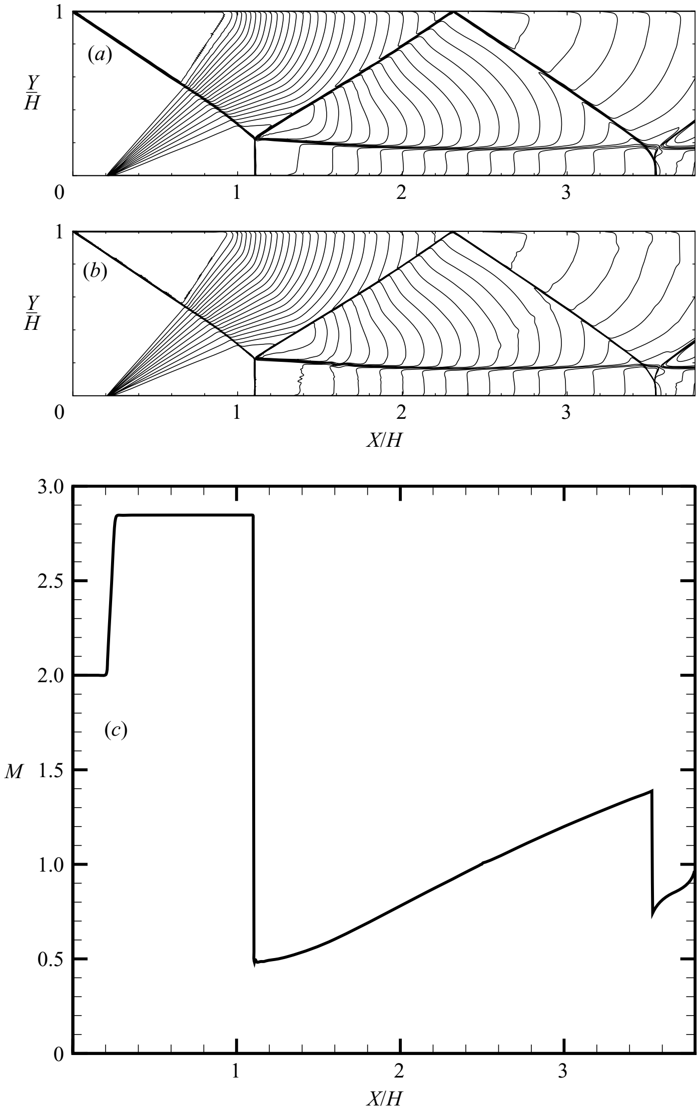

FIGURE 9. Density contours for Mach reflection, with a Mach-2.0 flow deflected through 20.44 degrees, i.e. 0.5 degrees above the detachment boundary of figure 6, with the expansion corner at $X/H = 0.2$: (*a*) coarse mesh; (*b*) standard mesh; (*c*) Mach-number distribution along the line $Y/H = 0.001$.

Mach-reflection studies the required low pressure is generated by the expansion wave from the trailing edge of the wedge used to generate the incident shock wave (e.g. Ben-Dor *et al.* 1999), as shown in figure 2(*b*). In the present study, reflection of the initial expansion wave from the upper surface of the duct back onto the streamtube is the equivalent mechanism. Thus the position and scale of the Mach stem depend critically upon the axial location of the expansion corner relative to the upper leading edge.

Figures 9(*a, b*) and 10 show perturbations from the regular-reflection result of figure 8(*b*). The operating points in the (M_1, δ_1)-domain are shown in figure 11. Figure 9 shows an increase of 1.0 degree from figure 8(*b*), so that the incidence

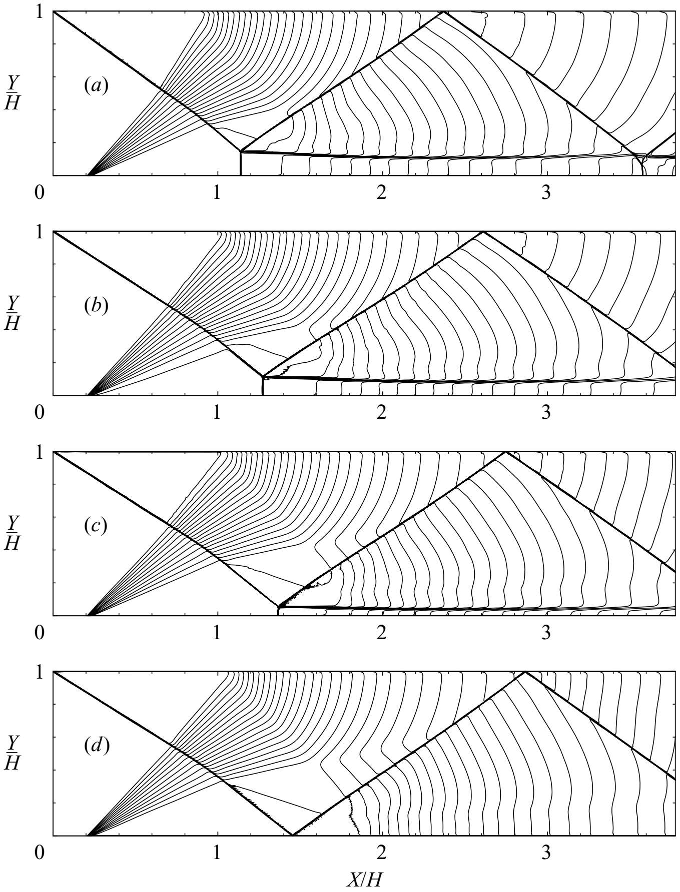

FIGURE 10. Density contours for Mach reflection of an incident flow perturbed from the Mach-2.0, 19.44 degrees incidence regular-reflection case of figure 8(*b*). (*a*) Incidence maintained at the original value and Mach number reduced to 1.92; (*b*) Mach number returned from the state shown in (*a*) to the original value; (*c*) Mach number held fixed and incidence reduced by 0.5 degrees; (*d*) further reduction in incidence by 0.5 degrees. These operating points are shown in figure 11.

is just 0.5 degrees above the predicted detachment criterion. The simulation was initialized with the output data from the regular reflection of figure 8, but the new flow conditions at the inflow boundary were enforced. Figures 9(*a*) and 9(*b*) are coarse-mesh and standard-mesh simulations and show a mesh insensitivity similar to that of the regular-reflection case of figure 8. A specific point to note is the behaviour of the reflected shock wave formed at the triple point. This reflects in turn from the upper surface of the duct back to the post-Mach-stem streamtube. The fact that it then penetrates through the streamtube up to the lower wall shows that the streamtube flow is fully supersonic at this position. A minimum-streamtube area – the sonic throat – has formed somewhat upstream of this impingement zone. This is further illustrated by figure 9(*c*), where the variation in Mach number with streamwise distance (for $Y/H = 0.001$) establishes a clear supersonic zone in the streamtube before the abrupt deceleration to subsonic flow at $X/H \approx 3.54$. Thus the impinging shock wave is unable to influence the position and scale of the Mach stem in this case.

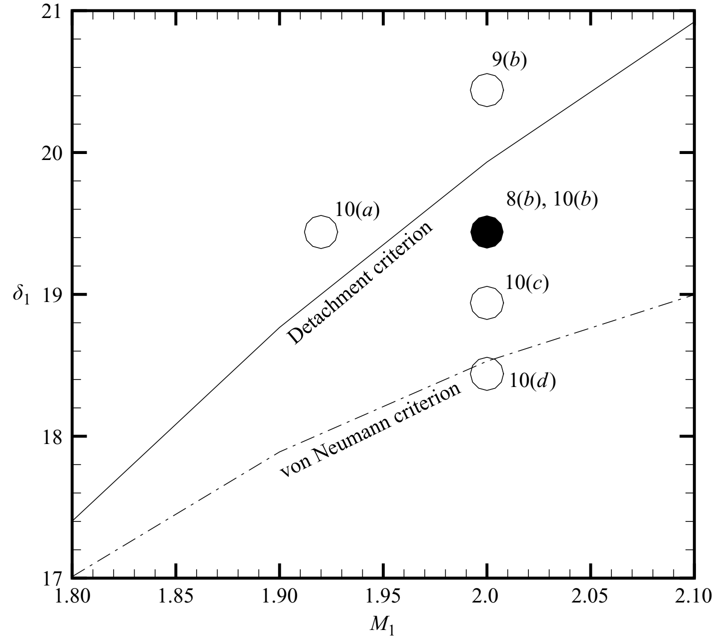

FIGURE 11. Detail in the (M_1, δ_1)-plane showing the test cases corresponding to parts of figures 8–10.

In figure 10(*a*) the situation is perturbed from the regular-reflection case of figure 8(*b*), crossing the 'detachment' boundary by a reduction in Mach number to 1.92 whilst maintaining constant flow deflection. Once more a stable Mach reflection is formed. Figure 10(*b*) corresponds to starting from the conditions of figure 10(*a*) and increasing the Mach number back to the initial value of 2.0. Thus figure 10(*b*) and figure 8(*b*) correspond to the same Mach number and incidence and demonstrate the dual-solution possibility and the possibility of hysteresis in the flow process. Figure 10(*b*) can also be produced by decreasing the incidence from the state illustrated in figure 9(*b*). Figures 10(*c*) and (*d*) show successive 0.5 degree reductions in flow deflection from the state of figure 10(*b*), with a return to regular reflection in figure 10(*d*) at an angle just below the predicted von Neumann criterion.

4.2. *Effect of streamwise positioning of the expansion corner,* $M_1 = 2.0$

Figure 12 shows the effect of the relative positioning of the lower-surface expansion corner. These simulations were all performed at Mach 2.0 and at 0.5 degrees above the detachment criterion. In each case a regular-reflection case (at 0.5 degrees below the detachment criterion) was generated, then the inflow boundary incidence was increased by 1.0 degree. Figure 12(*g*) illustrates the closest approach of the (projected) impingement position of the incident shock wave to the expansion corner. That is, it represents the least 'off-design' movement from the classical shock-on-shoulder case of figure 1. Figures 12(*a–c*) appear as conventional Mach-reflection cases. They include the trajectory of the critical Mach line (evaluated from the CFD), which originates in the initial expansion fan and terminates on the boundary of the post-Mach-stem streamtube at the sonic throat. All these figures also include the computed sonic line, superimposed upon the density contours, and clearly seen in figures 12(*a–c*) as positioned at the foot of the impinging critical Mach line. For Figure 12(*d*) the

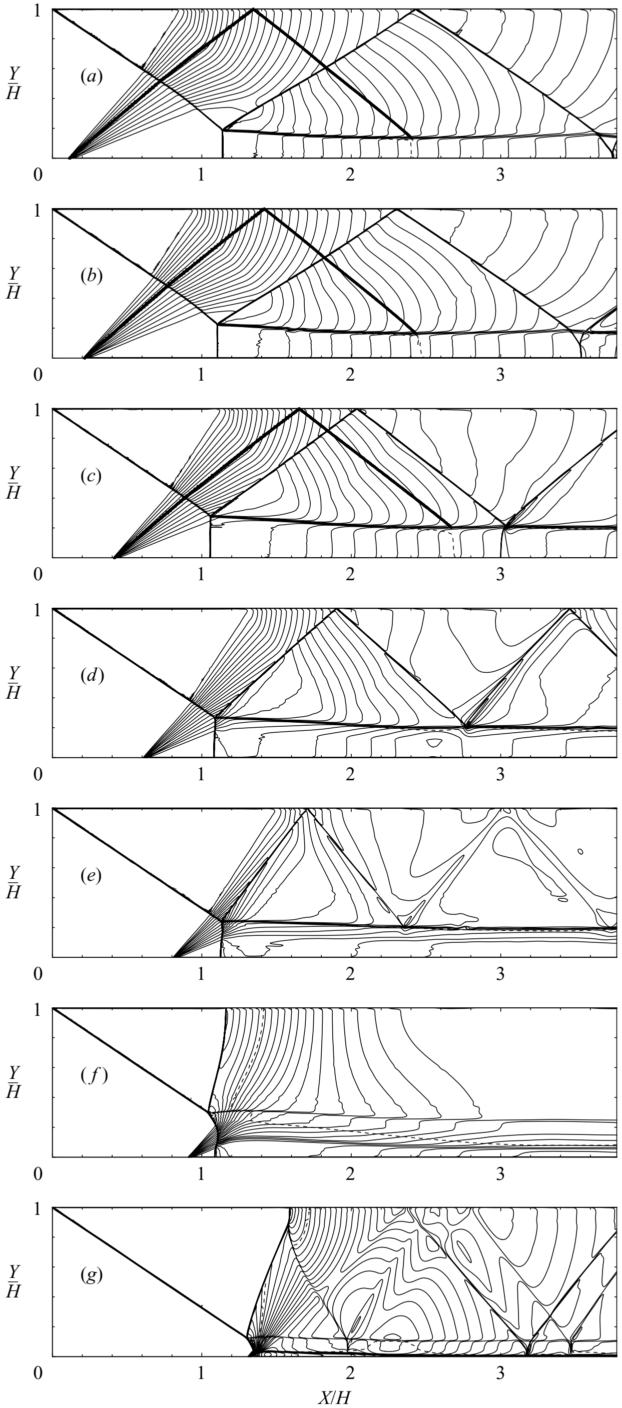

FIGURE 12. Density contours for Mach reflection of an incident flow at Mach 2.0 and 20.44 degrees deflection, showing the effect of moving the expansion-corner relative to the upper-surface leading edge, to the following values of X/H: (*a*) 0.1; (*b*) 0.2; (*c*) 0.4; (*d*) 0.6; (*e*) 0.8; (*f*) 0.9; (*g*) 1.3. The trajectory of the critical Mach line impinging upon the sonic throat is shown by the bold line in the first three cases. The dashed curve indicates the location of the sonic line.

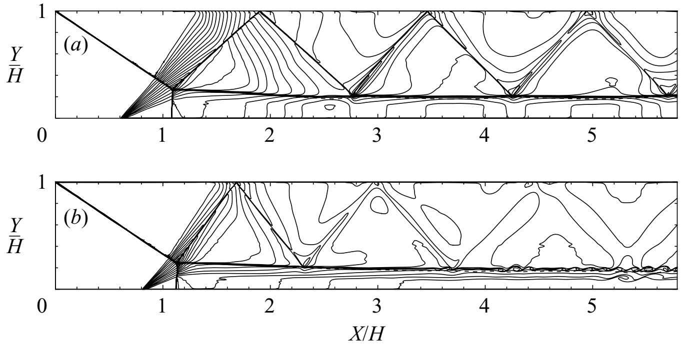

FIGURE 13. Simulations showing the insensitivity of the flow field to the location of the outflow boundary. (*a*) A repeat of figure 12(*d*), with the outflow boundary moved downstream by a further two units in X/H. (*b*) A repeat of figure 12(*e*).

reflected shock wave from the triple point, having itself been reflected from the upper surface of the duct, overtakes the critical Mach line so that no sonic streamtube condition is achieved. The streamtube is subsonic up to the outflow boundary. A feedback process is now possible where movement of the triple point, communicated to the slipstream via the trajectory of the reflected shock wave, can provide a further influence on the Mach stem. Because the exit flow is subsonic (the lowest value is approximately 0.82), figure 13 is used to judge any flow-field sensitivity to the position of the outflow boundary. In this case figure 12(*d*) is repeated, with the streamwise extent of the flow field extended by a further two units in X/H. Apart from a few differences in detail, figures 13(*a*) and 12(*d*) are virtually identical. In a similar manner figure 13(*b*) shows that the result of figure 12(*e*) is also insensitive to the location of the downstream outflow boundary.

With rearwards movement of the expansion corner, the triple point progressively moves from behind the expansion wave (figures 12*a*, *b*), through it (figures 12*c*–*d*) and in front of it (figures 12*f*, *g*). Between figures 12(*e*) and 12(*f*) there is a marked difference in the reflected wave, which corresponds to a change from the 'weak' to the 'strong' option. Using the exact MOC computations, three-shock modelling shows that this change must occur in the expansion fan when the triple point is at a polar angle of about 40 degrees, measured from the expansion corner. This is illustrated by figure 14, which shows polar plots for various triple-point locations with respect to the expansion fan, the solid and dashed lines giving the pressure versus flow deflection immediately downstream of, respectively, the reflected wave and the transmitted wave (i.e. the Mach stem). Only the upper part of the Mach-stem curve – the strong-shock solution – is appropriate; for the reflected wave, both branches, upper (strong) and lower (weak) are possible. The intersection between the two curves identifies the triple point TP. Figure 14(*a*) shows the case with the triple point located behind the expansion fan, with a weak solution for the reflected wave. In front of the expansion wave, figure 14(*c*), only the strong option is possible for the reflected shock. Figure 14(*b*) corresponds to the location in the expansion wave, at $\phi \approx 40$ degrees, at which the transition from a weak to a strong reflected shock wave occurs. Figure 12(*e*) happens to be close to this condition. The sonic line in figure 12(*f*) shows that the subsonic flow downstream of the reflected shock wave has been accelerated quickly to supersonic speed. There is also a complex stratification below the slipstream from

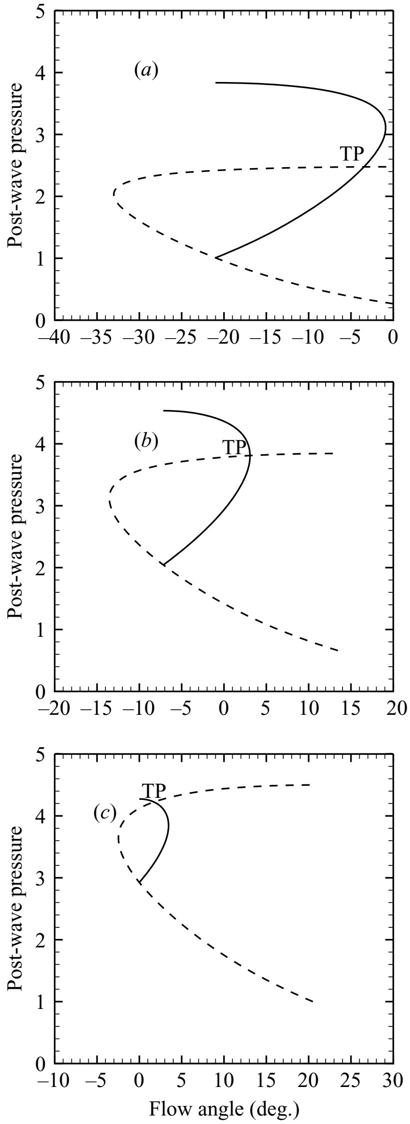

FIGURE 14. Post-shock-wave conditions at the triple point TP, showing pressure vs. flow angle for $M_1 = 2.0$ at 20.45 degrees (initial-flow incidence at 0.5 degrees above the detachment criterion). The solid and dashed lines, respectively, refer to the conditions downstream of the reflected wave and the transmitted wave (i.e. the Mach stem). (*a*) Triple-point formation behind the expansion fan; (*b*) triple-point formation in the expansion fan at an angle $\phi = 39.65$ degrees relative to the lower-surface expansion corner; (*c*) triple-point formation in front of the expansion fan.

the triple point, the sonic-line locus showing that the bulk of the flow at the exit boundary ($Y/H \geqslant 0.08$) is supersonic.

Previously, figures 8(*b*) and 10(*b*) showed the dual-solution possibility for the Mach-2.0 case, with the expansion corner positioned at $X/H = 0.2$. A similar result is demonstrated in figure 15, for the extreme case of figure 12(*g*), with the expansion corner located at $X/H = 1.3$. This shows two simulations, both at 0.5 degrees below the detachment criterion. Figure 15(*a*) was initiated with the data of figure 12(*g*) but

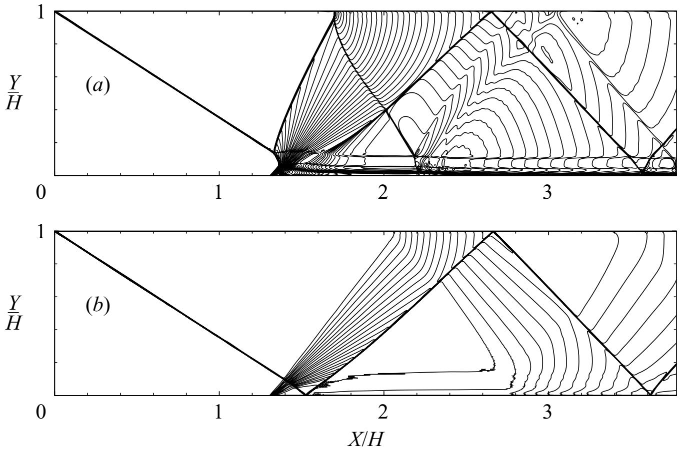

FIGURE 15. CFD simulation showing the dual-solution possibility for incident flow at Mach 2.0, incidence 0.5 degrees below the detachment criterion and the expansion corner at $X/H = 1.3$. (*a*) Mach reflection achieved with the flow initialized using data from figure 12(*g*) but with reduced inflow angle, and (*b*) regular reflection produced by an impulsive start of the flow.

with the inflow incidence reduced, whereas figure 15(*b*) is a regular reflection result produced by an impulsive initialization of the flow field with the required initial conditions imposed everywhere in the domain.

4.3. *Effect of variation in M_1 at 0.5 degrees above the detachment criterion*

In figure 16 the expansion corner is fixed at $X/H = 0.1$ and the Mach number is progressively increased, always maintaining the flow deflection at 0.5 degrees above the appropriate detachment condition. Figure 12(*a*), at Mach 2.0, was essentially the first run in this series and only this and figure 16(*a*), at Mach 2.1, provide interactions with the triple point behind the expansion fan. These cases, which are similar in character to the conventional wedge-generated Mach reflection, are referred to, for convenience, as 'type-1' cases. Once the triple point has entered the expansion fan, the interactions are referred to as 'type-2'. Up to figure 16(*c*) the reflected shock wave from the upper surface can penetrate fully through the streamtube because the flow is locally supersonic, as is seen by the positioning of the sonic line in the figures. Above this Mach number a two-layer nature of the streamtube becomes apparent, the reflected shock wave penetrating only through the supersonic upper layer, essentially that part of the flow downstream of the segment of the Mach stem that has interacted with the expansion fan, whereas the lower layer remains fully subsonic. Again the sonic line in the figures shows how the respective subsonic and supersonic zones are established. There is a gradual evolution of the flow field up to $M_1 = 2.7$ (figure 16*f*) but by $M_1 = 2.75$ (figure 16*g*) a large-scale transition has occurred, to what is referred to as a 'type-3' interaction. Clearly the flow is not steady, characterized partly by the roll-up of the various slip surfaces. More basically, there is an overall large-scale motion, albeit at long time scales; the computation is actually presented at this stage since, at later times, the Mach-stem segment at the lower wall propagated up to the expansion corner and the computation was stopped.

A similar phenomenon – but now producing a nearly steady end state with only slight flow-field oscillations – is seen in figure 17 for the case with the expansion corner located at $X/H = 0.4$. Even for the first of this sequence; see figure 17(*a*), the

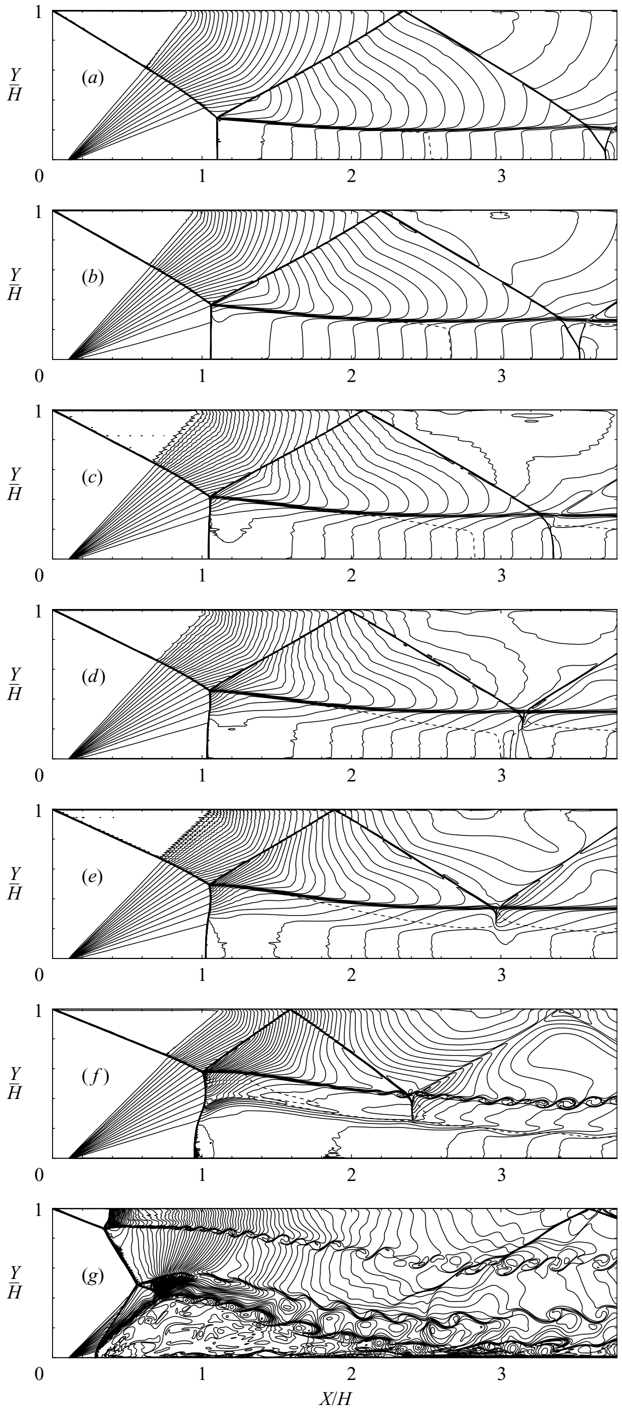

FIGURE 16. Density contours. The expansion corner is at $X/H = 0.1$ and the incident flow is at 0.5 degrees above the detachment condition. (*a*) $M_1 = 2.1$; (*b*) $M_1 = 2.2$; (*c*) $M_1 = 2.3$; (*d*) $M_1 = 2.4$; (*e*) $M_1 = 2.5$; (*f*) $M_1 = 2.70$; (*g*) $M_1 = 2.75$. In each figure, the dashed curve indicates the location of the sonic line.

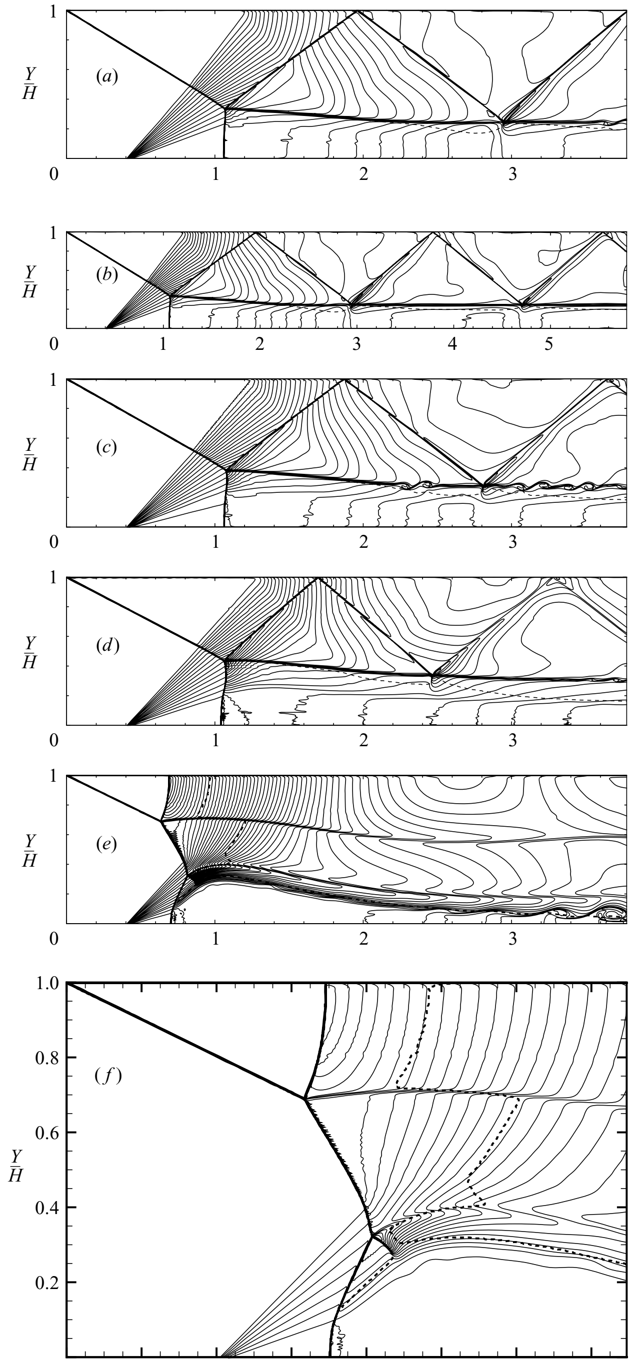

FIGURE 17. Density contours for Mach reflection with the expansion corner at $X/H = 0.4$ and the incident flow at 0.5 degrees above the detachment criterion. (*a*) $M_1 = 2.1$; (*b*) extended mesh version of (*a*); (*c*) $M_1 = 2.2$; (*d*) $M_1 = 2.3$; (*e*) $M_1 = 2.4$; (*f*) detail for (*e*), with 10% contour intervals in ρ/ρ_∞. The dashed curve indicates the location of the sonic line.

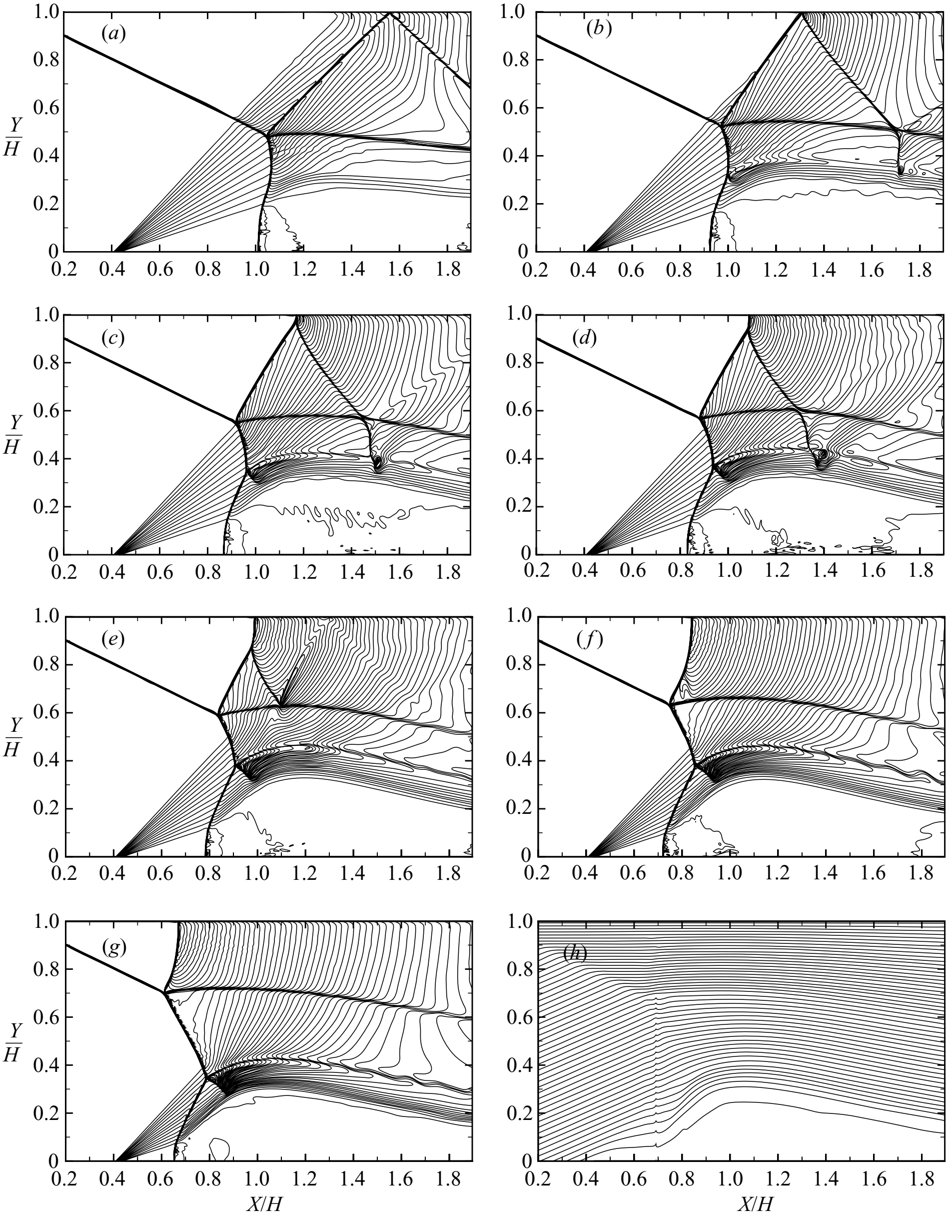

FIGURE 18. Density contours showing the time development of the change to type-3 Mach reflection, for the case of figure 17(*d*). Panels (*a*) to (*g*) are density contours at the following times TU_1/H after initiation of the computation: 19.6, 44.0, 53.8, 58.7, 63.6, 68.5, 73.4. (*h*) The final streamlines, in 50 equal intervals in mass flux.

post-Mach-stem streamtube is subsonic up to the exit plane. Figure 17(*b*) repeats this case, with a streamwise extension of the domain, showing once more an insensitivity of the flow field to the location of the exit boundary. In the sequence of figure 17, the transition from a recognizable Mach reflection to a situation where the shock system has migrated close to the expansion corner takes place in the range $2.3 \leqslant M_1 \leqslant 2.4$. Figure 18 shows the time-history of the transition from figure 17(*d*) to figure 17(*e*),

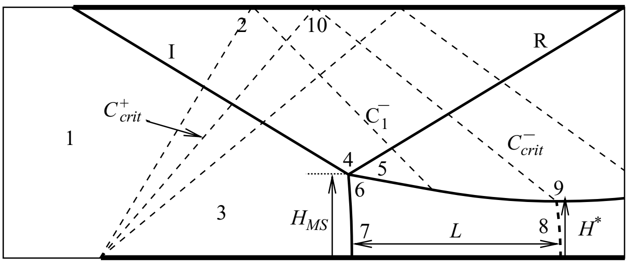

FIGURE 19. Schematic showing the interaction of the reflected expansion wave with the slipstream downstream of the triple point, for the type-1 case.

obtained by enforcing (at time $T = 0$) an $M_1 = 2.4$ inflow boundary condition (with inflow incidence 0.5 degrees above the corresponding detachment criterion) upon the $M_1 = 2.3$ flow state of figure 17(*d*). By figure 18(*a*) the interaction has caused the Mach stem to form an inflexional profile. This develops as a small segment of 'weak' shock that, by figure 18(*b*), has focused to form a second triple point, with the post-shock supersonic flow terminated by a developing secondary shock wave. Later times show a progressive enlargement of the weak-shock segment. Below the new triple point the interaction with the expansion fan generates large upwards flow deflections. In consequence, the flow that passes through the wall-segment of the Mach stem (i.e. essentially that part of the Mach stem from the wall up to the trailing edge of the expansion fan) experiences very large flow divergence – also illustrated by the 'streamlines' in figure 18(*h*) for the nearly steady case of figure 17(*e*) – and an associated deceleration to very low velocities. Downstream of the maximum-height position the streamtube constricts very substantially again, so that the flow accelerates from near-stagnant conditions to near-sonic speed at the outflow boundary of the domain in figure 17(*e*). Above this particular streamtube the flow has divided into three further streamtubes, demarcated by the slipstreams from the two triple points. Each of these experiences a sub-to-supersonic acceleration, as shown in detail in figure 17(*f*), the large divergence of the flow in the bottom streamtube generating the constriction for the necessary throats in the upper layers. The fact that figure 18(*g*) shows that the wall Mach stem is forwards of the location for the Mach stem in figures 17(*e*, *f*) is an indication that, in the development from figure 17(*d*) to figure 17(*e*), the shock-wave system overshoots its final equilibrium position.

5. Discussion

Figure 19 shows a simple schematic for the type-1 Mach reflection. Basically, three geometrical factors control the size and location of the Mach stem; firstly, the ratio of the height of the Mach stem, H_{MS}, to the height of the sonic throat, H^*; secondly, the horizontal spacing between the incident shock wave I and the critical Mach line C^-_{crit}, since the triple point and the sonic throat must lie on the first and second of these two trajectories, respectively; thirdly, the ratio of the length of the subsonic streamtube L and the height of the Mach stem H_{MS}. These various factors will be considered next, in §§5.1–5.3 for the special case of the type-1 Mach reflection.

5.1. *Streamtube width at the Mach stem and sonic throat: type-1 interaction*

From the initial expansion-wave conditions and the MOC predictions for the incident shock-wave trajectory, all conditions at points 3–7 in figure 19 are known exactly. Assuming one-dimensional streamtube motion, the average conditions at point 8 and

M_1	δ_1	X_{LE}/H	H_{MS}/H	H^*/H	H_{MS}/H^*	L/H	g	L/H_{MS}	Seen in
2.0	20.44	0.1	0.190	0.140	1.366 (1.371)	1.261	0.24	6.62 (7.43)	figure 12(*a*)
2.0	20.44	0.2	0.227	0.166	1.372 (1.371)	1.326	0.30	5.84 (7.06)	figure 12(*b*)
2.0	20.44	0.4	0.280	0.204	1.373 (1.371)	1.614	0.39	5.76 (6.62)	figure 12(*c*)
2.1	21.42	0.1	0.278	0.198	1.408 (1.395)	1.419	0.32	5.10 (5.50)	figure 16(*a*)
2.2	22.25	0.1	0.364	0.255	1.426 (1.418)	1.58	0.28	4.34 (4.70)	figure 16(*b*)
2.0	20.44	0.1	0.069	0.049	1.408 (1.371)	0.558	0.19	8.09 (7.73)	figure 21(*a*)
2.5	24.02	0.1	0.2175	0.146	1.490 (1.473)	0.868	0.20	3.99 (3.57)	figure 21(*b*)
2.75	24.88	0.1	0.246	0.159	1.550 (1.507)	0.940	0.08	3.82 (3.36)	figure 21(*c*)

TABLE 1. Computed scale of the subsonic streamtube downstream of the Mach stem for various type-1 interactions, all taken with the initial flow deflection at 0.5 degrees above the predicted detachment criterion for regular-to-Mach transition. H^* and H_{MS} are the heights of the sonic throat and the Mach stem respectively. L is the streamwise length from the Mach stem to the sonic throat. The numbers in parentheses are taken from one-dimensional streamtube theory for H_{MS}/H^* and from (5.4) for L/H_{MS}. The fractional length g of the subsonic streamtube, for impingement of the first C^- characteristic, was determined by inspection of the CFD solutions.

hence the ratio H_{MS}/H^* can be calculated. Table 1 shows the close agreement between this value and the values obtained from the CFD simulations.

5.2. *Origin of the critical Mach wave in the initial expansion fan and the length of the subsonic section of the post-Mach-stem streamtube: type-1 interaction*

Figures 12(*a–c*) showed the origin of the trajectory of the critical Mach line in the initial expansion wave. This location can also be inferred using simple flow-field modelling based on figure 19. The required pressure matching between points 8 and 9, and the fact that points 5 and 9 are linked by isentropic flow, means that the conditions at point 9 can be specified completely. With zero flow deflection δ_9 at point 9, the Riemann variable $(\nu + \delta)_9$ can also be specified, where ν is the Prandtl–Meyer angle. Along the C^-_{crit} characteristic the variable $\nu + \delta$ must reduce, as a result both of the entropy increase along its path from the upper wall at point 10 to the slipstream at point 9 (see the characteristic equations (2.1) and (2.2)) and also of its passage across the reflected shock wave. For zero entropy change, $\nu + \delta$ would be invariant along the Mach line; as a first-order approximation, it is assumed that, since points 2 and 10 have the same entropy, as also do points 5 and 9,

$$(\nu + \delta)_{10} - (\nu + \delta)_9 \approx (\nu + \delta)_2 - (\nu + \delta)_5. \tag{5.1}$$

Here, the conditions at points 2 and 5 are known exactly. In a similar manner, the initial value of $(\nu - \delta)_{crit}$ on the critical C^+_{crit} characteristic in the initial expansion wave is approximated as

$$(\nu - \delta)_{crit} - (\nu - \delta)_{10} \approx (\nu - \delta)_1 - (\nu - \delta)_2. \tag{5.2}$$

Noting that $\delta_{10} = 0$,

$$(\nu - \delta)_{crit} \approx (\nu + \delta)_9 + (\nu - \delta)_1 - (\nu - \delta)_2 + (\nu + \delta)_2 - (\nu + \delta)_5. \tag{5.3}$$

It is then easy to determine the ray angle, in the initial expansion wave, for the critical Mach line, C^+_{crit}. Figure 20 shows how this depends upon M_1 and includes the values determined directly from the CFD of figures 12(*a*), 16(*a*) and 16(*b*). The agreement between the CFD data and the result (5.3) is so close that the approximate treatment of the entropy-variation term is fully justified. Figure 20 shows that, for all

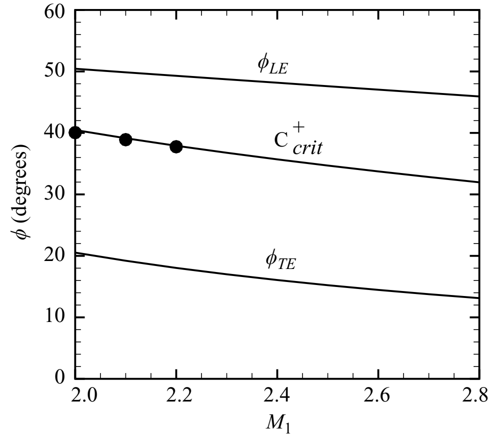

FIGURE 20. Identification of the C^+_{crit} Mach line in the initial expansion wave, showing the ray angles ϕ_{LE} and ϕ_{TE} (relative to the expansion corner) of the leading- and trailing-edge Mach lines, the prediction of the ray angle for the critical Mach wave C^+_{crit} using (5.3) (solid line) and the CFD data (solid symbols) taken from figures 12(*a*), 16(*a*) and 16(*b*).

Mach numbers, the C^+_{crit} Mach line is contained centrally within the initial expansion wave, so that the reflected wave expansion is always sufficiently strong to provide a sonic throat in the post-Mach-stem streamtube. That it does not, apart from at the lower Mach numbers and the most forward positions of the expansion corner, is a consequence of the progressive movement of the triple point into the expansion fan and the associated forwards movement of the impingement position of the reflected shock wave on the slipstream.

Extending this analysis to determine the spacing between the incident shock wave and the C^-_{crit} wave – the primary driver for the length ratio of the subsonic streamtube, L/H – is difficult and it is easier to consider the outcomes from the CFD modelling. An increase in X_{LE}/H (i.e. a rearwards movement of the expansion corner) must automatically increase the wave spacing; this is also achieved by increased M_1, because of the increased sweep of the waves. Both these effects are seen in the CFD predictions for L/H in table 1 (the rearwards movement of X_{LE}/H in rows 1, 2 and 3 of the table and the increased M_1 values in rows 1, 4 and 5).

A demonstration of how the scale L/H of the Mach reflection can be radically changed by altering the spacing of the incident shock wave and the C^-_{crit} Mach line, can be provided by deliberately generating a centred expansion wave, originating on the upper surface of the channel at a position forwards of the impingement region of the primary expansion wave. This is illustrated for the cases of figures 12(*a*) ($M_1 = 2.0$), 16(*e*) ($M_1 = 2.5$) and 16(*g*) ($M_1 = 2.75$), which are type-1, type-2 and type-3 interactions respectively. Equation (5.3) can be used to predict the upper-surface turning angle required to (just) provide the appropriate critical C^- condition; the values obtained are approximately 6.5, 9.3 and 10.2 degrees, respectively, for the three cases. Figure 21 presents these cases using an upper-surface turning angle approximately 50% larger than the predicted value to ensure proper establishment of a supersonic flow in the post-Mach-stem streamtube. The centred expansion was implemented in the computations by deflecting the upper solid boundary of the domain abruptly through the required angle and maintaining this new surface inclination for the remainder of the domain up to the downstream outflow boundary;

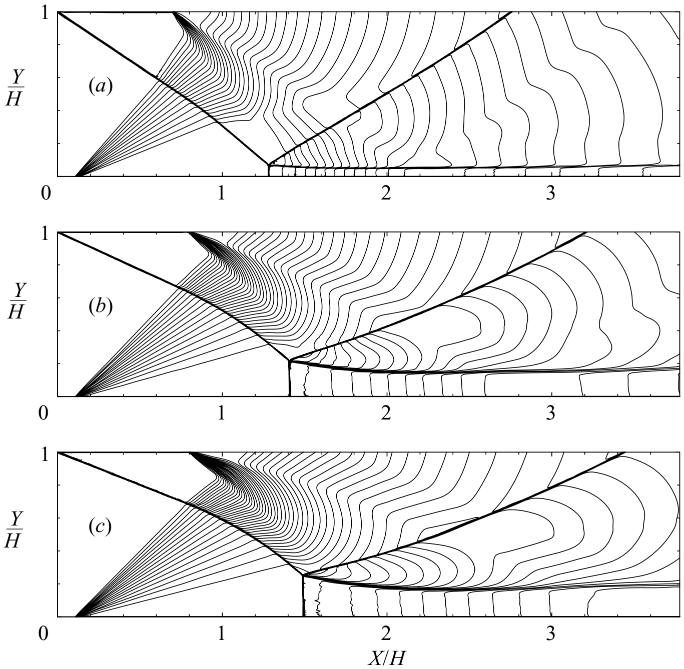

FIGURE 21. Effect on the scale of the Mach stem, for the cases of figures 12(*a*), 16(*e*) and 16(*g*), of an expansion corner positioned on the upper-surface of the channel. (*a*) $M_1 = 2.0$, with the upper-surface expansion corner (9 degrees) positioned at $X/H = 0.7$. (*b*) $M_1 = 2.5$, with the upper-surface expansion corner (12 degrees) positioned at $X/H = 0.8$. (*c*) $M_1 = 2.75$, with the upper-surface expansion corner (15 degrees) again positioned at $X/H = 0.8$.

thus the height of the computational domain extends beyond the upper boundary shown in these figures. The expansion corner was located as far forwards as possible, to ensure the earliest possible interaction of the expansion wave with the slip surface, whilst avoiding the situation where it actually catches up with (and therefore attenuates) the incident shock wave. The three results each now provide a type-1 Mach reflection. The various scales associated with the subsonic streamtube, for these three cases, are also included in table 1.

5.3. *Length-to-height ratio of the subsonic streamtube and the scale of the Mach stem: type-1 interaction*

Table 1 includes the CFD data for the ratio of the streamtube length L and the height of the Mach stem, H_{MS}. The larger this ratio the shallower the streamtube, for a given spacing between the incident shock wave and the critical Mach line, and the lower probability therefore that the triple point will then enter the expansion fan. The table clearly shows that the ratio reduces rapidly with increased Mach number. A geometric approximation, based upon the schematic of figure 19, assumes that the initial slip-surface trajectory is a straight line, determined by the slipstream slope $\delta_{5,6}$ predicted at the triple point, and that once the first Mach line (C_1^-) impinges on the slip surface the trajectory is a circular arc up to the impingement of the critical Mach line (C_{crit}^-) at the sonic throat, where the local flow-deflection angle δ_9 is zero. Of course, this geometric model does not satisfy the pressure matching required between the external supersonic flow and the internal subsonic flow (although the correct matching at the Mach stem and at the sonic throat has already been enforced). Li & Ben-Dor

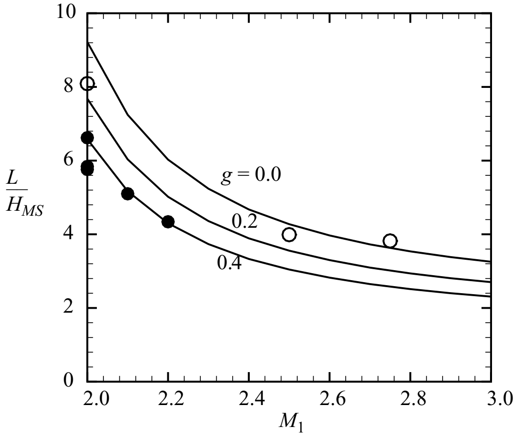

FIGURE 22. Variation in the ratio of the length of the subsonic streamtube segment and the height of the Mach stem. The solid lines correspond to the geometrical model of (5.4), for g values 0.0, 0.2 and 0.4. The individual symbols are the results from the CFD cases listed in table 1, with open symbols in the range $0 \leqslant g \leqslant 0.2$ and solid symbols in the range $0.2 \leqslant g \leqslant 0.4$.

(1997) presented a model for wedge-generated Mach reflection, where the slipstream trajectory followed the predicted streamlines of the incident expansion wave, which also provided no general pressure matching, however. Assuming that H_{MS}/H^* is given by one-dimensional modelling, if the first Mach line of the expansion wave, C_1^-, impinges at a distance gL from the Mach stem then the geometrical model gives

$$\frac{L}{H_{MS}} \approx \frac{(H^*/H_{MS} - 1)}{(1-g)(1-\cos\delta_{5,6})/\sin\delta_{5,6} + g\tan\delta_{5,6}}. \tag{5.4}$$

Equation (5.4) is plotted in figure 22. It also includes values from the specific CFD cases, which are listed in table 1. The CFD results clearly support the trends suggested by (5.4), showing that L/H_{MS} reduces both with later impingement of the C_1^- Mach wave (i.e. with increased g) and also with increased Mach number, through the direct effect on the deflection $\delta_{5,6}$ of the slipstream at the triple point (note that the deflection is downwards, making the deflection angle negative). It is this reduction in L/H_{MS} that quickly propels the triple point into the expansion fan.

5.4. *Movement of the triple point into the expansion wave and the transition from type-2 to type-3 reflection*

The previous sections showed various factors that increase the scale of the Mach stem for type-1 interactions. An increased Mach number slightly elongates the subsonic streamtube and strongly increases its width-to-length ratio H_{MS}/L. Rearwards movement of the expansion corner elongates slightly the post-Mach-stem subsonic streamtube and reduces the clearance between the foot of the Mach stem and the trailing edge of the expansion fan. For these reasons it was only possible to produce type-1 interactions for low Mach numbers and for expansion-corner positions that are far forwards. The definition of type-1 and type-2 interactions is essentially one of convenience, however, defined by whether the triple point is behind or within the expansion wave. The first main effect of enlargement of the Mach stem is that eventually the reflected shock wave from the triple point reflects back onto the slipstream before the C_{crit}^- Mach wave reaches it. At this stage a sonic throat is no longer achieved in the post-Mach-stem streamtube, or rather in the central portion

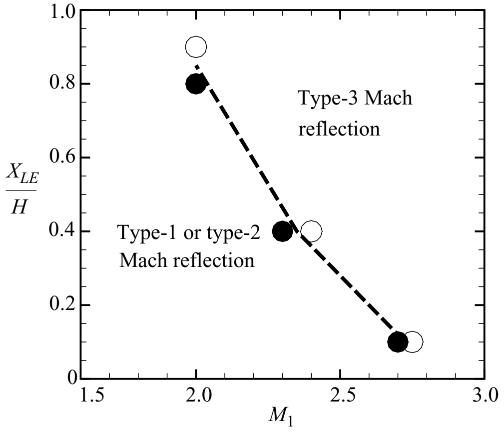

FIGURE 23. Domain for M_1 vs. X_{LE}/H, where X_{LE} is the position of the lower-surface expansion corner, for a flow deflection 0.5 degrees above the detachment transition angle, showing the boundary between type-1 or type-2 and type-3 Mach reflection. The solid symbols are type-2 simulations, the open symbols are type-3.

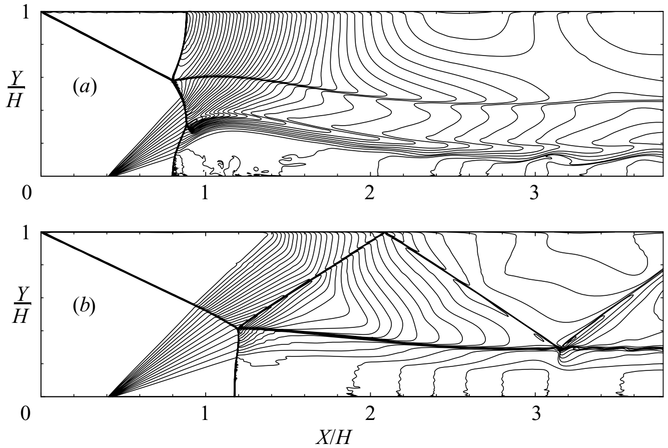

FIGURE 24. Assessment of a possible hysteresis process for the case of figure 17(*d*). (*a*) M_1 reduced to 2.3, whilst maintaining incidence at 0.5 degrees above the Mach-2.3 detachment criterion; (*b*) M_1 maintained at 2.4, whilst reducing incidence by 1.0 degrees to 0.5 degrees below the detachment criterion.

because the streamtube stratification of the type-2 flow means that the outer part might remain supersonic. In itself this does not make an immediate contribution to the transition to type-3 Mach reflection, but the difference between the cases of figures 16(*f*) and 16(*g*), or between figures 17(*d*) and 17(*e*) (or the time sequence of figure 18) shows the importance of the progressive forwards movement of the impingement position of the reflected shock wave on the post-Mach-stem streamtube. The behaviour of the shock-wave reflection at the upper surface of the duct is also significant. For the cases given in figure 18 this shows a regular-to-Mach reflection transition, and it is possible that this transition would exhibit a hysteresis if the process were reversed. In figure 23 the preceding computations are used to define the M_1 versus X_{LE}/H domain for the transition from type-2 to type-3 Mach reflection. To assess any type-2–type-3 hysteresis, figure 24 shows two computations, both starting with the $M_1 = 2.4$ (type-3) result of figure 17(*e*). In the first computation the inflow conditions are altered to reduce M_1 to 2.3, with a new incidence 0.5 degrees above the detachment criterion for Mach 2.3; it shows that a type-3 reflection is still preserved, and may be compared with the type-2 conditions of figure 17(*d*). A further reduction in M_1 to 2.2, however, produced the same flow solution as figure 17(*c*). This effect has not been explored further, but the boundary in figure 23 probably represents an upper Mach-number limit for type-2–type-3 transitions. In the second case, figure 24(*b*), M_1 is maintained at 2.4 but the flow deflection is reduced, so that it is 0.5 degrees below the detachment condition. In this case the flow reverts to type-2 Mach reflection, but the dual-solution possibility is retained since regular reflection can obviously be produced at these conditions also.

The effect of an increasing flow deflection on the type-3 interaction has not been studied beyond the cases presented. Several other points should be emphasized, however. Firstly, computations were stopped when the wall segment of the Mach stem approached the expansion corner so that no assessment was made as to when the shock system might propagate upstream of the expansion corner and 'unstart' the duct flow. Secondly, the flow processed by the Mach stem – figures 16(*g*) and 17(*e*) – experiences a large divergence and a very substantial deceleration to produce a large 'bubble' of nearly stagnant flow. The peak of this bubble corresponds with the sub-supersonic throats generated in the upper streamtubes, as shown in figure 17(*f*). There is every reason to believe that the bubble is an actual inviscid effect, but there would be every likelihood in a real viscous flow that it would result in a flow recirculation, i.e. a flow 'separation' but one that has origins in the inviscid flow-field behaviour. Thirdly, type-1 and type-2 computations generally achieved a steady state, but this was not the case for the type-3 simulations. Figure 17(*e*) showed only a slow, small-amplitude, backwards–forwards movement, so that the figure is probably a good representation of a mean state. Figure 16(*g*) is clearly unsteady, however, both in terms of the shear layer rollup, which is not of immediate consequence, and also the large-scale overall motion.

6. Conclusions

There are several results of special significance. Firstly, there is a large difference between the permitted deflection angles for the shock-on-shoulder design case and those angles that permit regular reflection to be maintained at off-design. Figure 6 would indicate that the maximum-design-angle case – at least theoretically – corresponds to the angle for shock detachment from the leading edge of the shock generator. Although an intake, for example, is unlikely to operate so close to the leading-edge detachment condition, maintaining flow deflections below the detachment criterion (possibly even below the von Neumann criterion) is potentially very restrictive and becomes increasingly so at high Mach numbers. The flow-field differences and potential hysteresis associated with the dual-solution processes also presents a significant phenomenon, not least for the high-speed intake flows which stimulated this investigation initially. The implication is that for a fixed flight condition different flow fields can develop, with subsequent alterations to combustor inlet conditions and flight performance. Secondly, there is a severe restriction on Mach number and expansion-corner position, shown by figure 23, if a large-scale perturbation of the type-3 interaction is to be avoided. At $M_1 = 2.0$ the shock-on-shoulder condition requires $X_{LE}/H \approx 1.5$ and this value increases with M_1. Avoidance of the type-3 interaction, however, means that the streamwise position of the expansion corner must be located increasingly close to the shock-generator leading edge as M_1

increases; essentially the compression generated by the upper-surface shock wave then becomes increasingly counteracted by the lower-surface expansion system, so that the compression effectiveness of the turning process reduces. Thirdly, the scale of the Mach reflection is clearly controlled by the reflected expansion wave and the positioning of this wave relative to the trajectory of the shock wave reflected from the triple point. This places significant constraints upon the permitted values of X_{LE}/H and M_1, because of the broad spatial spread of the reflected expansion wave. As figure 21 demonstrated, however, the scale of the Mach reflection can be radically altered by deliberate generation of a further expansion wave. This might provide the elements of a control mechanism as long as the total geometric configuration is considered, in order to ensure that the compression ability of the duct inlet flow is not compromised.

A final comment should be made on the fact that the results – CFD, MOC and simple analytical modelling – are inviscid and therefore provide a specific limiting case. One reason for ensuring that numerically induced total pressure losses were minimal for the flow through the initial expansion wave (near the wall), was the observation from early computations with a very coarse mesh (coarser than any presented here) that the type-2–type-3 transition occurs at a lower Mach number, and with a tendency for the wall shock to move more rapidly up to the expansion corner, than for the fine mesh results presented throughout this paper. It has to be assumed that viscous effects would accentuate this process.

REFERENCES

Azevedo, D. J. & Liu, C. S. 1989 Engineering approach to the prediction of shock patterns in bounded high-speed flows. *AIAA J.* **31**, 83–90.

Ben-Artzi, M. & Falcovitz, J. 1984 A second-order Godunov-type scheme for compressible fluid dynamics. *J. Comput. Phys.* **55**, 1–32.

Ben-Dor, G., Elperin, T., Li, H. & Vasiliev, E. I. 1999 The influence of downstream pressure on the shock wave reflection process in steady flows. *J. Fluid Mech.* **386**, 213–232.

Ben-Dor, G., Ivanov, M., Vasiliev, E. I. & Elperin, T. 2002 Hysteresis processes in the regular reflection ↔ Mach reflection transition in steady flows. *Prog. Aerospace Sci.* **38**, Nos 4–5, 347–387.

Chpoun, A., Passerel, D., Li, H. & Ben-Dor, G. 1995 Reconsideration of oblique shock wave reflection in steady flows. Part 1. Experimental investigation. *J. Fluid Mech.* **301**, 19–50.

Henderson, L. F. & Lozzi, A. 1975 Experiments on transition of Mach reflection. *J. Fluid Mech.* **68**, 139–155.

Henderson, L. F. & Lozzi, A. 1979 Further experiments on transition of Mach reflection. *J. Fluid Mech.* **94**, 541–549.

Hillier, R. 1991 Numerical modelling of shock wave diffraction at a ninety degrees convex edge. *Shock Wave J.* **1**, 89–98.

Hornung, H. G., Oertel, H. & Sandeman, R. J. 1979 Transition Mach reflexion of shock waves in steady and pseudosteady flow with and without relaxation. *J. Fluid Mech.* **90**, 541–560.

Hornung, H. G. & Robinson, M. L. 1982 Transition from regular to Mach reflection of shock waves Part 2. The steady-flow criterion. *J. Fluid Mech.* **123**, 155–164.

Ivanov, M. S., Markelov, G. N., Kudryavtsev, A. N. & Gimelshein, S. F. 1998 Numerical analysis of shock wave reflection in steady flows. *AIAA J.* **36**, 2079–2086.

Li, H. & Ben-Dor, G. 1995 Oblique-shock/expansion interaction –analytical solution. *AIAA J.* **34**, 418–421.

Li, H. & Ben-Dor, G. 1997 A parametric study of Mach reflection in steady flows. *J. Fluid Mech.* **341**, 101–125.

Liepmann, H. W. & Roshko, A. 1957 *Elements of Gas Dynamics*. Wiley.

Molder, S. 1979 Particular conditions for the termination of regular reflection of shock waves. *CASI Trans.* **25**, 44–49.

von Neumann, J. 1943 Oblique reflection of shock. *Collected Works*, vol. 6, pp. 238–299. Pergamon.